Weather influence on passive microwave brightness temperatures

STIG M. LØVÅS, IRENE RUBINSTEIN and CHRISTIAN ULSTAD

Sea ice charts produced using spaceborne passive microwave observations are used on routine basis at several ice forecasting centres and during sea ice research campaigns. The capability of passive microwave sensors to monitor the earth, regardless of cloud cover or daylight, and the 1400 km swath width (SSM/I) make these sensors well suited not only for ice forecasting but also for providing information needed for planning northern oceanic routes. The retrieval of sea ice parameters is carried out by utilizing 37 and 19 GHz brightness temperatures measured by Special Sensor Microwave Imager (SSM/I) on the Defense Meteorological Satellite Program (DMSP) platform. The ice type identification uses a-priory established signature brightness temperatures for each ice type. The algorithm generating the sea ice information contains some climatological information on the weather dependence of the observed brightness temperature. A comparison between passive microwave (SSM/I) retrieved ice parameters and ice maps from the Norwegian Meteorological Institute (DNMI) indicates that the weather correcting procedure within the algorithm may need regionalized input. The correlation of variability of the observed brightness temperatures with the weather changes has to be derived prior to introducing any corrections to the existing algorithms. The observed brightness temperatures contain information not only about the ice surface but also the atmospheric contribution. One of the crucial tasks is to establish a technique for flagging changes on the ice surface in order to segregate them from the atmospheric influence on the passive microwave signal. To obtain more knowledge about the effects of regional weather on the retrieval of sea ice parameters, local climatological information from DNMI has been compared with the SSM/I ice charts. This paper focuses on the outcome of this comparison and how regional atmospheric information can be used in the retrieval of sea ice information from passive microwave data.

S. M. Løvås, SINTEF NHL, N-7034 Trondheim, Norway; I. Rubinstein, Institute for Space and Terrestrial Science (ISTS), York University, 4850 Keele Street, North York, Ontario, Canada M3J 3K1; C. Ulstad, Norwegian Meteorological Institute (DNMI), P.O. Box 43 Blindern, N-0313 Oslo, Norway.

Introduction

The remote sensing of sea ice with active and passive microwave sensors has become an indispensable tool to the polar research community. The traditional sources of sea ice information are now augmented with the data obtained from interpretating Special Scanning Microwave Imager (SSM/I) multi spectral passive microwave observations.

The study of physical properties of the earth's surface and atmosphere with microwave radiometry became possible with the launch of COSMOS-243 (Basharinov et al. 1971). Single frequency Nimbus-5 Electrically Scanning Microwave Radiometer (ESMR) observations from 1972 to 1976 provided for the first time a set of global observations that allowed sea ice studies on a synoptic scale (Staelin et al. 1973; Zwally 1984). Since June 1978, multispectral dually polarized observations (Scanning Multichannel Microwave Radiometer on SEASAT and later on NIMBUS-7, Special Scanning Microwave Imager on DMSP (Hollinger et al. 1987)) of the earth microwave radiance have been used in monitoring the extent and physical properties of the sea ice cover and other geophysical parameters.

Algorithms for translating the microwave measurements into sea ice cover parameters evolved after 1978, when Scanning Multichannel Microwave Radiometer (on NIMBUS-7) data were used to establish the ice monitoring capabilities of passive microwave sensors. At the Institute of Space and Terrestrial Science at York University, an algorithm known as the AES/York Algorithm has been developed. The algorithm utilizes the SSM/I channels 19 and 37 GHz (both polarizations) to produce sea ice information (Total ice concentration, First year ice fraction, Old ice fraction and Thin/New ice fraction) and wind speed and cloud cover information for ice-

free pixels. (Ramseier et al 1989; Hollinger 1991). The AES/York Algorithm is calibrated against ground truth measurements from several ice-infested waters. Observations from several surveys (also in the Barents Sea) have shown generally good agreement with the total ice concentration values provided by the algorithm. A study on the variations in ice type fraction in the Barents Sea based on SSM/I ice charts from September 1988–May 1989 (Løvås et al. 1991) showed that the amount of old ice and thin ice varied in reverse proportion. The existence of old ice is far more important to the design and operation of vessels and marine structures than new ice, hence a correct discrimination between old ice and new ice is important.

Materials and methods

Data sets

The data used in this project were acquired from March 22 through April 10 1992 and are as follows:

SSM/I data from the US Defence Meteorological Satellite Program.

AVHRR data from the NOAA-11 satellite.

Atmospheric data from the atmospheric Limited Area Model, LAM50S, of the Norwegian Meteorological Institute (DNMI).

Passive Microwave Multispectral Measurements were obtained from Civilian Navy Data Distribution Services Computer (CNODDS) in Monterey, California and processed at the Earth Observations Laboratory of the Institute for Space and Terrestrial Science in Toronto, Canada. The dates of SSM/I imagery are listed in Table 1.

Advanced Very High Resolution Radiometer data were obtained from and processed at the Tromsø Satellite Station (low resolution) and DNMI (full resolution). The full resolution imagery has been processed and histogram enhanced at the Meteorological Institute SATellite image processing system MISAT (MISAT is an I²S based image processing system with an IVAS station as display unit and VAX support. The system has been developed by Spacetec

Table 1. Remotely sensed data and derivatives.

Date (1992)	SSM/I		AVHRR		Ice analyses
	Time	Orbit	Time (Low res.)	Time (Full res.)	
23 March	06:57	cc1636		06:29	●
	08:38	dd1637	09:39		
24 March	06:44	cc1650	09:27	12:52	
25 March	06:32	cc1664	09:13	06:52	
26 March	06:19	cc1678	10:43	06:29	●
27 March	07:48	cc1693	10:32		
28 March	09:17	cc1708	10:20		
29 March			10:08		
30 March	07:10	dd1735	09:56	05:06	●
31 March	06:56	dd1749			
1 April	08:25	dd1764	11:12	04:42	
2 April	06:31	cc1777	11:00	08:11	●
3 April	06:47	cc1791			
	10:25	cc1792	09:09		
4 April	06:35	cc1805	10:37		
5 April	07:57	cc1820	10:25		
6 April	09:24	dd1834	10:13		
7 April	07:37	cc1848			
	10:52	cc1849	10:01		
8 April	08:59	dd1863			
9 April	07:10	dd1878			
10 April			09:26		

A/S, Tromsø, in cooperation with DNMI). The dates of AVHRR imagery are listed in Table 1.

The atmospheric data were obtained from the LAM50S atmospheric model of DNMI. Due to the "spin-up"-time when starting a large numeric model, realistic values on the humidity quantities are fully obtained after six hours of running. Therefore the data used here are twelve hour prognoses. The following quantities were used:

Cloud cover in percent (4 levels)

Relative humidity (7 levels)

Convective precipitation (accumulated during six hours)

Frontal precipitation (accumulated during six hours)

Temperature at 2 m level (above the model topography)

A rectangle containing Hopen, Bjørnøya and the southern part of Spitsbergen was chosen with 4 of a total of 48 grid points as corners. The time resolution is twelve hours, and the spatial resolution is 50 km.

The sea-ice analyses were obtained directly from the daily update of the sea ice conditions in the MISAT system. They are produced by drawing curves on the displayed imagery, using the graphical system in MISAT. The dates of analysis are listed in Table 1.

Retrieval of sea-ice parameters from spaceborne passive microwave observations

The microwave radiation from the earth is a complex function of the temperature, physical composition and properties of the earth surface altered by the absorption, emission and scattering from the atmosphere. The quantitive determination of the environmental parameters is obtained from a limited set of relatively noisy microwave radiation measurements. In general these measurements are not sufficient for unique determination of the environmental parameters without some a priori empirical knowledge and mathematical models on the relationship between these parameters and measured radiometric temperatures. The empirical information is used to impose limits within which these parameters can vary. The accuracy of the retrieved information is therefore affected by the noise in the empirical data and the uncertainties in assumptions used in model equations.

The brightness temperature, T_B, is defined as

the temperature T in K (Kelvin) to which a black body must be raised in order to radiate with the same intensity. The brightness temperatures measured by the sensor, for any of the sensor channels, contain contributions from the earth, atmosphere and space radiation. Assuming non-precipitating atmosphere, the observed brightness temperature can be expressed as:

$$T_B = T_{Bs}\exp(-\tau) + T_1 + (1 - e)T_2\exp(-\tau) + (1 - e)T_c\exp(-2\tau) \qquad (1)$$

where T_{Bs} is the surface radiation, τ is the atmospheric opacity, T_1 is the atmospheric upwelling radiation, e is the surface emissivity, T_2 is the downwelling atmospheric radiation and T_c is the cosmic space contribution. The atmospheric components, under assumptions stated above, can be expressed in terms of an atmospheric mean temperature T_a. In polar regions, for the frequencies used in the algorithms, the atmospheric opacity is small, but not negligible. Due to the noncoherent nature of the natural microwave emission from the surface, the surface radiation can be written as a sum of contributions from different ice types and open water. Equation 1 can be rewritten for the following scenarios:

1) Single channel, dually polarized observations;
2) Dual frequency, same polarizations for both channels.

(1): The surface radiation term, if C represents the fraction of the footprint covered with ice, can be written as:

$$T_{BsP} = CT_{BiP} + (1 - C)T_{BwP} \qquad (2)$$

where subscript P represents vertical or horizontal polarization, T_{BiP} is ice signature brightness temperature and T_{BwP} is the open ocean signature brightness temperature. The surface emissivity can also be written as a sum of the emissivities from ice fraction and open ocean:

$$e_p = Ce_{iP} + (1 - C)e_{wP} \qquad (3)$$

Substitution of Equations 2 and 3 into Equation 1 yields Equations 4 and 5 for vertical and horizontal polarizations respectively:

$$T_{BV} = \exp(-\tau)[CT_{BiV} + (1 - C)T_{BwV} + 1 \\ (Ce_{wV} - Ce_{iV})T_2] + T_1 + (Ce_{wV} - Ce_{iV})T_c \\ \times \exp(-2\tau) \qquad (4)$$

$$T_{BH} = \exp(-\tau)[CT_{BiH} + (1 - C)T_{BwH} + \\ (Ce_{wH} - Ce_{iH})T_2] + T_1 + (Ce_{wH} - Ce_{iH})T_c \\ \times \exp(-2\tau) \qquad (5)$$

Taking the difference between Equations 4 and 5 and neglecting contribution from space yields following expression for C:

$$C = [\exp(\tau)DT_{BVH} - DT_{Bw}]/[DT_{Bi} - DT_{Bw} + (De_w - De_i)T_2] \quad (6)$$

where:

$$DT_{BVH} = T_{BV} - T_{BH} \quad (7)$$

$$DT_{Bi} = T_{BiV} - T_{BiH} \quad (8)$$

$$DT_{Bw} = T_{BwV} - T_{BwH} \quad (9)$$

$$De_w = e_{eV} - e_{wH} \quad (10)$$

$$De_i = e_{iV} - e_{iH} \quad (11)$$

General form of Equation 6 can be written as:

$$C = ADT_{BVH} + B \quad (12)$$

Coefficients A and B are calculated using Equation 6. Equation 12 (when the assumption is made that the difference between vertical and horizontal sea ice brightness temperatures is independent of ice type) is known as Hughes algorithm. From this equation one can analyse dependence of the total ice cover estimate on the variability in atmospheric conditions. The variability of DT_{Bi} with the ice types present within the field of view can also influence the accuracy of the calculations. If the weather conditions are used as an input to calculations of A and B, this type of an algorithm can be tuned to be very sensitive to the sea ice presence within the pixel. In the absence of meteorological information, it can lead to false classification of an ice-free pixel for a wind-roughened ocean or an overcast sky. Errors in the calculated concentrations can also occur if an inappropriate value of DT_{Bi} is selected as a threshold value for the ice presence within a pixel. The dependence of the coefficients A and B on selection of typical optical opacity and DT_{Bi} is shown in Figs. 1 and 2.

(2): For any two channels (frequency f_1 and f_2) with different sensitivities to the atmospheric conditions and different sea ice and open ocean signatures, Equations 4 and 5 can be written as follows:

$$T_{B1} = \exp(-\tau_1)[CT_{Bi1} + (1 - C)T_{Bw1} + (Ce_{w1} - Ce_{i1})T_{21}] + T_{11} + (Ce_{w1} - Ce_{i1})T_{c1} \times \exp(-2\tau_1) \quad (13)$$

$$T_{B2} = \exp(-\tau_2)[CT_{Bi2} + (1 - C)T_{Bw2} + (Ce_{w2} - Ce_{i2})T_{22}] + T_{12} + (Ce_{w2} - Ce_{i2})T_{c2} \times \exp(-2\tau_2) \quad (14)$$

Assuming that only two ice types are present within the pixel (C_{F1} concentration of ice type one, C_{F2} concentration of the second ice type) and C_w is the fraction of open water, the Equations 13 and 14 can be solved for the ice fractions under the following constraint:

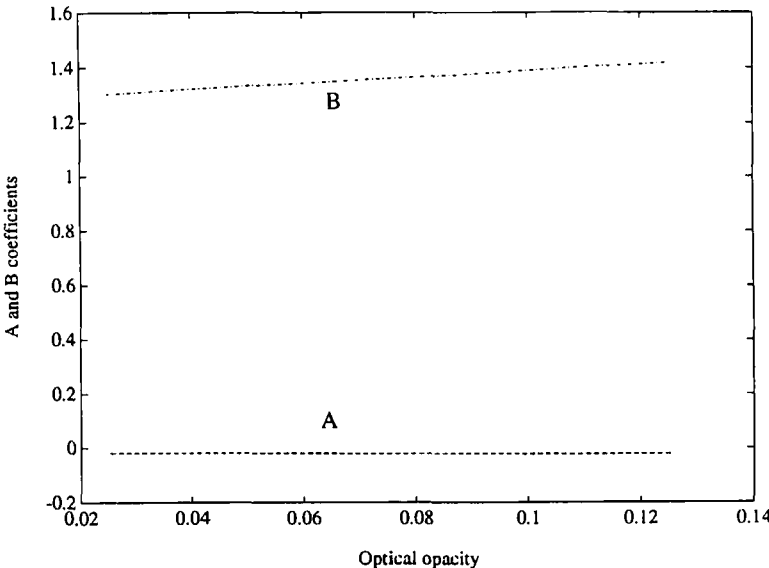$$C_{F1} + C_{F2} + C_w = 1 \quad (15)$$

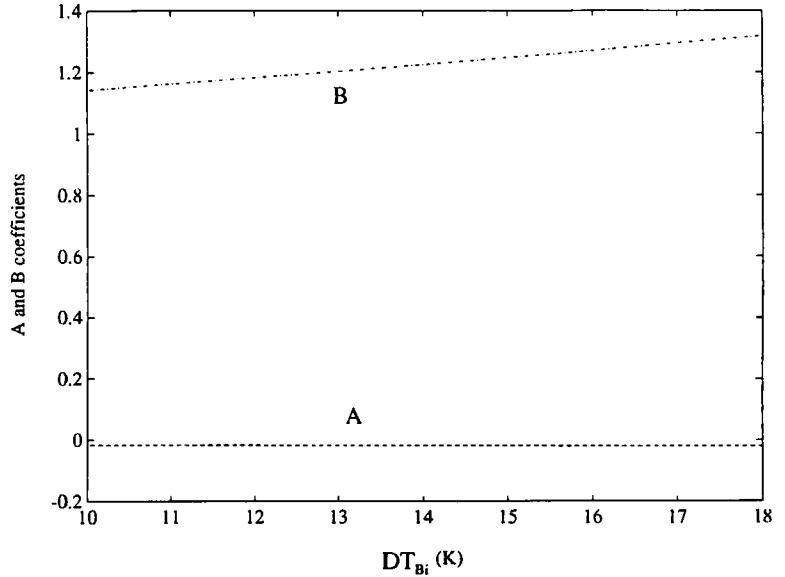*Fig. 1.* Dependency of coefficients A and B on optical opacity.

Fig. 2. Dependency of coefficients A and B on DT_{Bi}.

Replacing $(1 - C)$ by $1 - C_{F1} - C_{F2}$, one can show that solutions for C_{F1} and C_{F2} can be written as:

$$C_{F1} = A_1 T_{B1} + B_1 T_{B2} + C_1 \qquad (16)$$

$$C_{F2} = A_2 T_{B1} + B_2 T_{B2} + C_2 \qquad (17)$$

$$C = C_{F1} + C_{F2} = A_C T_{B1} + B_C T_{B2} + C_C \qquad (18)$$

Coefficients A_1, B_1, C_1, A_2, B_2, C_2, A_C, B_C, C_C are obtained from Equations 13 and 14. Good estimates of ice type fraction depends on validity of these coefficients. Hence, there is a need for ground truth from different areas and seasons. So far there has only been a few SSM/I ground thruth surveys in the Barents Sea. Such ground thruth measurements can easily be combined with other surveys into the ice-covered areas and would provide calibration data to improving the retrieval of Barents Sea ice parameters.

Equation 15 explains some of the reasons for the old/new ice fluctuations mentioned in the Introduction. If F_2 (the second ice type) is classified as old ice, then no new ice fraction can be calculated. If F_2 does not meet the old ice criteria, then C_{F2} is the new ice fraction. It can be shown that A_C, B_C, C_C are almost independent of optical opacity, whereas the dependence of A_1, B_1, C_1, A_2, B_2, C_2 on τ leads to the uncertainty in old and first year ice type fraction estimates (Rubinstein 1986).

Atmospheric influence on the retrieval of sea ice parameters

The atmospheric influence on the observed brightness temperatures, and therefore on the retrieved information, can be evaluated by varying the values for the transmittance of the atmosphere and the atmospheric radiation. For non-precipitating clouds the optical opacity τ can be calculated using the values of the attenuation coefficient, κ_1, by water clouds and fog as reported by Haroules & Brown (1969):

$$\tau = \kappa_1 \cdot m_v / 4.34 \qquad (19)$$

The parameter m_v is the water content of clouds in g/m^3. The atmospheric contribution can be estimated using the following approximation (Swift et al. 1984):

$$T_1 = (1 - \exp(-\tau)) \cdot (1.12 \cdot T_{cloud} - 50)$$

We will describe the atmospheric influence on the passive microwave algorithms that contain linear combinations of the observed brightness temperatures. Due to the regional and seasonal variabilities of the ice signatures, the AES/YORK algorithm contains several ice brightness temperature testing routines. Clustering of observations containing data representative to different regions is used to define the range of pure signature classes.
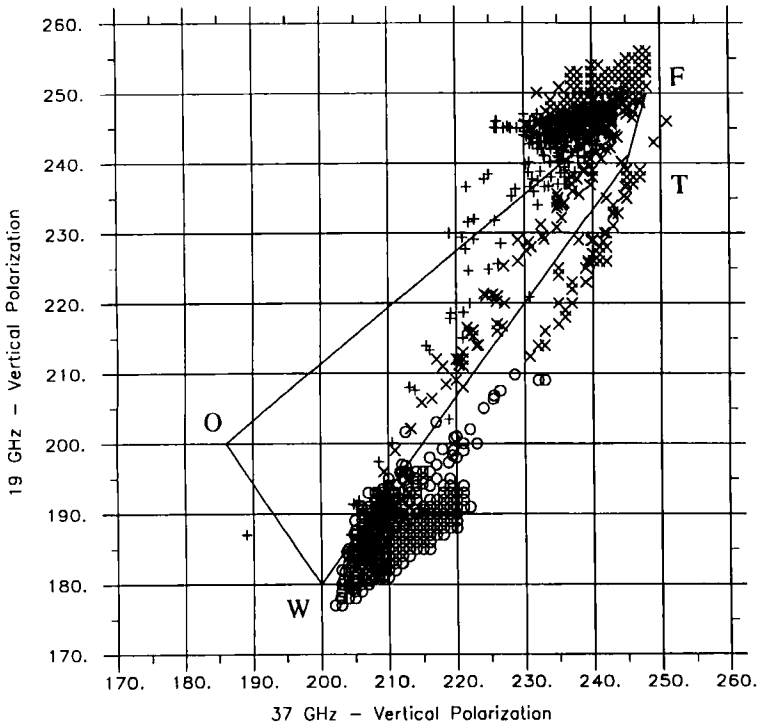
SSM/I Brightness Temperatures

Fig. 3. Scatter plot of T_{v19} vs. T_{v37} for Old Ice (+), Thin Ice (×) and Cloud Cover (○) footprints in the Western Barents Sea in March/April 1992. The polygon (OWTF) shows the valid area for ice footprints when no atmospheric contribution is present.

Pixels containing mixtures of pure classes can be identified as such if they are located within the limits of the following lines (Fig. 3): points along the OF line contain old and first year ice, while open ocean and first year ice mixtures are assumed to be along the WF lines. The WT line defines criteria for water plus new ice pixels. Fig. 3 shows several brightness temperatures outside the "ice" area. The cloud cover data points (o) can be separated into two groups. One group are pixels that are ice free, and changes in brightness temperatures are weather induced. For a calm ocean, the brightness temperature T_{v37} can reach 220 for overcast sky (no rain), while T_{v19} can be 195. Hence, drawing a line from W (the open ocean point) with a slope of 0.75 will separate the two groups. Data points below this line is considered ice free, while data points between this line and the WF line probably contain (new/thinner) ice.

Pixels can erroneously be classified as old ice (+) due to different footprint sizes at 19 GHz (50 Km) and 37 GHz (30 Km). This is more likely to happen for areas where there are changes in ice concentrations (i.e. diffuse ice to pack ice).

The 19 GHz channel will be seeing some of the higher concentrations (higher brightness temperatures) as compared to 37 GHz. If 19 GHz brightness temperatures are higher than 37 GHZ, the algorithm may declare that old ice is present. Resampling the SSM/I data for all channels to represent the same size of footprints will remove some of the ice type classification errors. High ice surface roughness, giving an increased capability to trap snow, can also be the cause for some of the ice to be classified as old.

Pixels not containing old ice can be identified by using the procedure described in the previous section. Since the calculated ice fractions should be real, positive numbers, special tests are performed on the incoming brightness temperatures if any of the calculated fractions are negative. One of the reasons for the fractions being negative is underestimation of the atmospheric opacity. New calculation of the ice fractions is then performed with optical opacity set to a different value. If that does not help, the pixel is classified as containing ice type of a positive fraction.

The operational usefulness of this algorithm is

enhanced by the following additional procedures: The brightness temperatures for the pixels identified as ice free are sent through an oceanic parameters algorithm. Ocean surface winds and cloud cover are calculated for these points. If any of the pixels contained ice and were not classified correctly, then the ocean algorithm will classify them as cloud covered (See Fig. 8)

The modular structure of this algorithm allows the use of each of the modules as an individual algorithm. This retrieval technique, although it appears to be more complex than other methods used, can be used for global and regional monitoring of the sea ice parameters. Equations 13 and 14 can be used for channels other than 19 and 37 GHz. The structure of the algorithm allows

Table 2. Evaluation of the AES/YORK algorithm performance (From Ramseier et al. 1989). The geographic areas included in the evaluation were the Beaufort Sea (old and first year ice), the Labrador Sea (first year ice) and the Gulf of St. Lawrence (first year ice). The time differences (±) between the satellite orbits and the corresponding validation data were less than 1 hour (class A), between 1 and 3 hours (class B) or between 3 and 6 hours (Class C).

Group category	Ice concentration		Ice edge displacement	
	Mean diff. (%)	95% CI[a]	Accuracy (km)	95% CI[a]
I Combined area				
Pooled	−8.9	0.9	−0.2	1.9
I-A, class A	−4.2	3.1	—	—
I-B, class B	−6.8	1.6	—	—
I-C, class C	−10.3	1.1	—	—
I-AB, class A + B	−6.3	1.4	—	—
I-1, ice formation	−9.1	1.3	−0.7	2.6
I-2, winter	−5.5	1.0	Same as III-2	Same as III-2
I-3, initial ice melt	Same as II-3	Same as II-3	Same as II-3	Same as II-3
I-4, ice melt	Same as II-4	Same as II-4	Same as II-4	Same as II-4
II Arctic				
Pooled	−8.6	0.9	−3.1	2.1
II-A, class A	0.4	2.3	—	—
II-B, class B	−7.1	1.8	—	—
II-C, class C	−10.0	1.2	—	—
II-AB, class A + B	−5.8	1.6	—	—
II-1, ice formation	−9.1	1.5	−5.1	2.9
II-2, winter	−1.5	0.5	—	—
II-3, initial ice melt	−5.1	2.7	−4.0	9.5
II-4, ice melt	−11.5	2.7	−4.3	3.6
III Gulf of St. Lawrence				
Pooled	10.1	1.6	7.4	4.2
III-A, class A	−12.1	4.5	—	—
III-B, class B	−5.8	2.5	—	—
III-C, class C	−12.1	2.2	—	—
III-AB, class A + B	−7.8	2.2	—	—
III-1, ice formation	−8.9	2.3	6.2	4.5
III-2, winter	−11.6	2.9	21.1	9.6
Ice fraction				
First year ice	−8.0	2.7		
Old ice	6.5	2.6		

[a]CI = Confidence interval

AIR TEMPERATURE
Western Barents Sea - 1992

PRECIPITATION
Western Barents Sea - 1992

CLOUD PERCENTAGE
Western Barents Sea - 1992

RELATIVE HUMIDITY
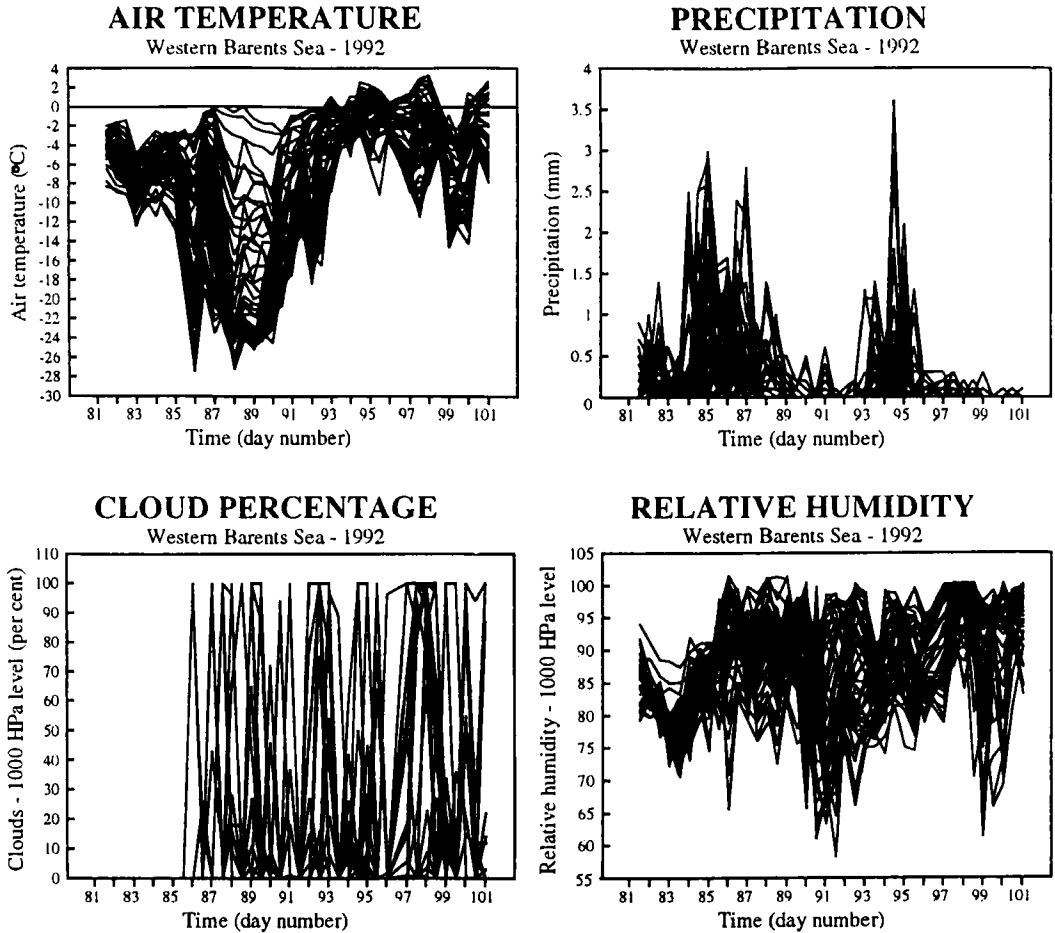### Western Barents Sea - 1992

Fig. 4. Air temperature (top left), precipitation accumulated over the last 6 hours (top right), cloud percentage (fog) at 1000 HPa level (bottom left), and relative humidity at 1000 HPa level (bottom right) from LAM50S model calculations.

switching to different channels since most of the constants are calculated from the signature brightness temperatures.

The performance of the algorithm described above was evaluated for different geographical regions using SSM/I data for 1987 and 1988 and sea ice information provided by the Canadian Atmospheric Environment Service (AES) Ice Centre. Results of the evaluation are shown in Table 2. The sea ice charts generated using this algorithm were used successfully for navigational support during sea ice research campaigns in the Greenland Sea, Barents Sea, Weddell Sea and North Atlantic Sea.

Results

Observations in the western Barents Sea, spring 1992

For some parameters of the atmospheric data generated for this study, Fig. 4 shows the variations as time series for all 48 grid points. The figures show a cold period from 25 March (Day 85) to 2 April. Prior to and early in this cold period there was some precipitation. During the period the cloud coverage varied. Generally, there was little fog, but there were some days with significant cloud percentages at the 300–850 HPa levels.
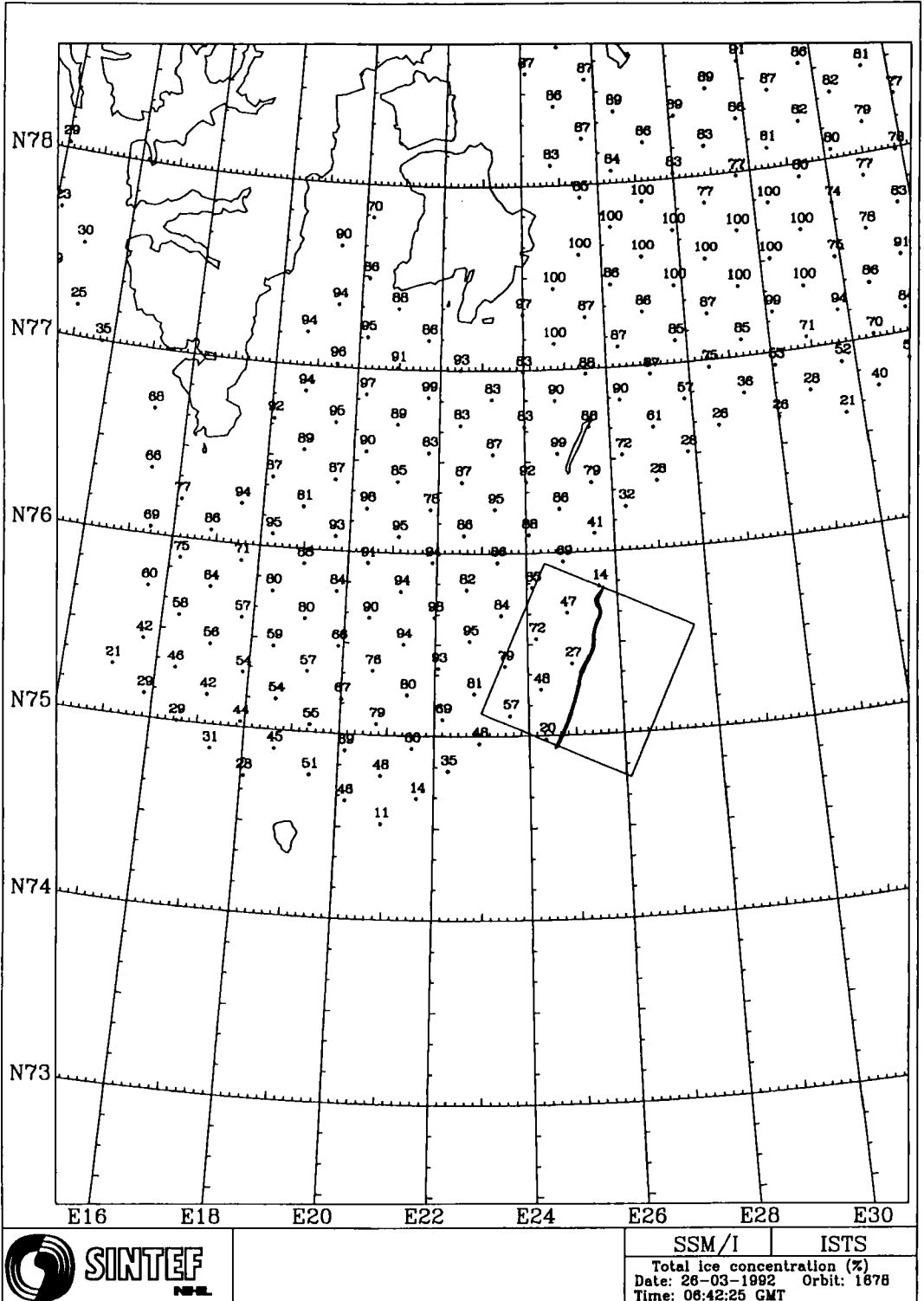
Fig. 5. SSM/I total ice concentration on 26 March 1992. The frame shows the location of the ERS-1 SAR scene (4 hours later). The thick line shows position of the ice edge in the SAR image.
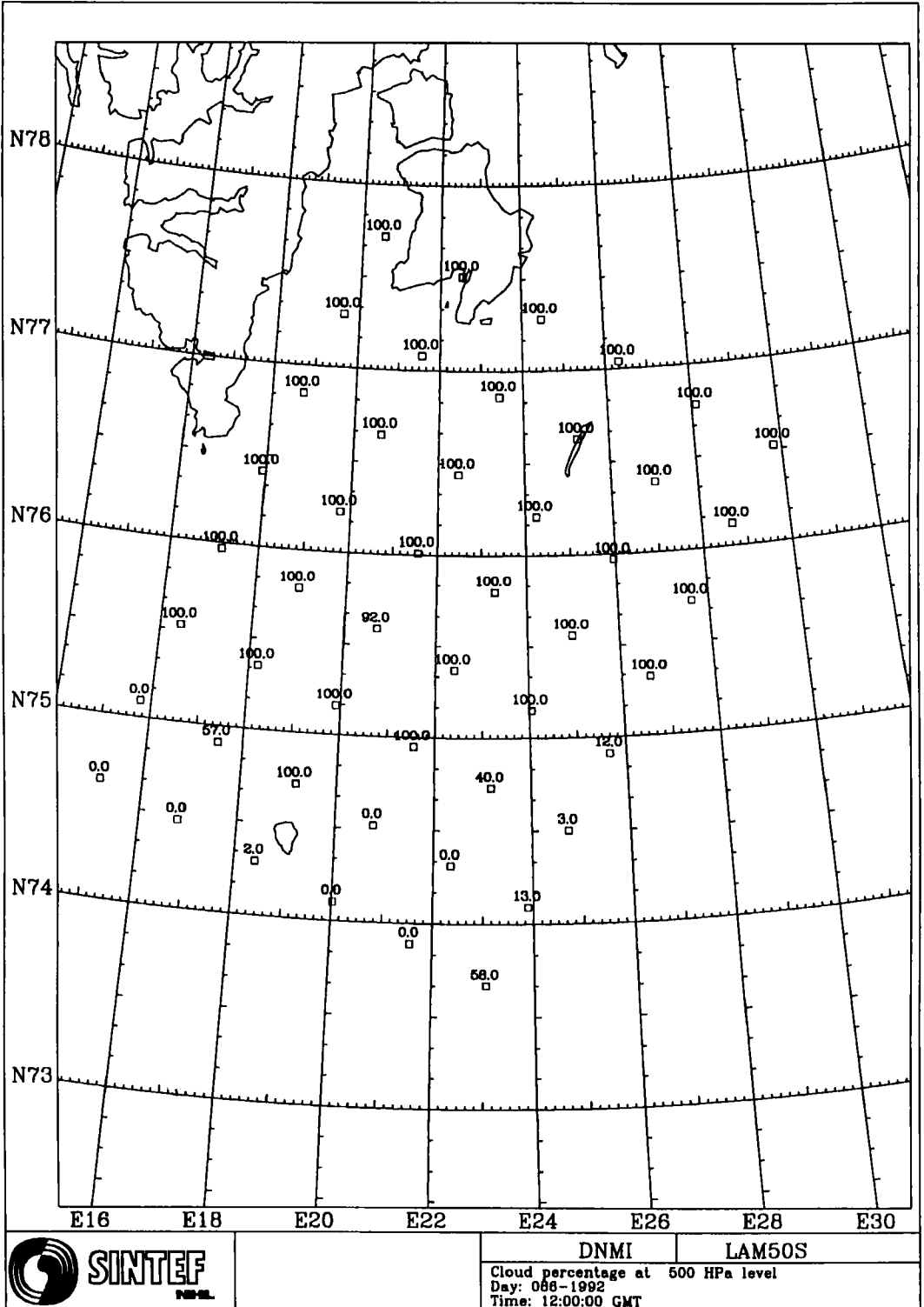
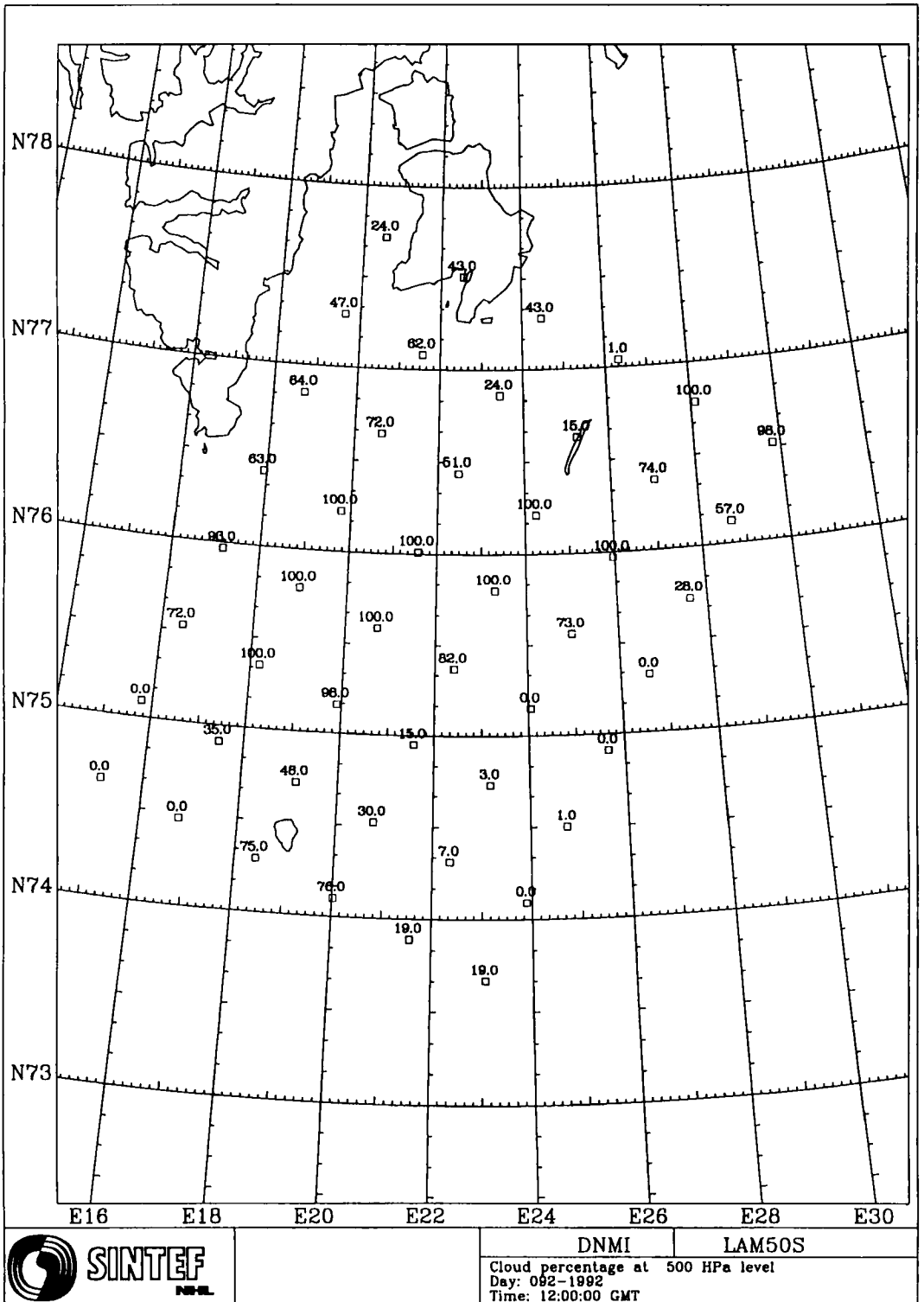Fig. 6. Cloud cover percentages at 500 HPa level on 26 March.

Fig. 7. Cloud cover percentages at 500 HPa level on 1 April.
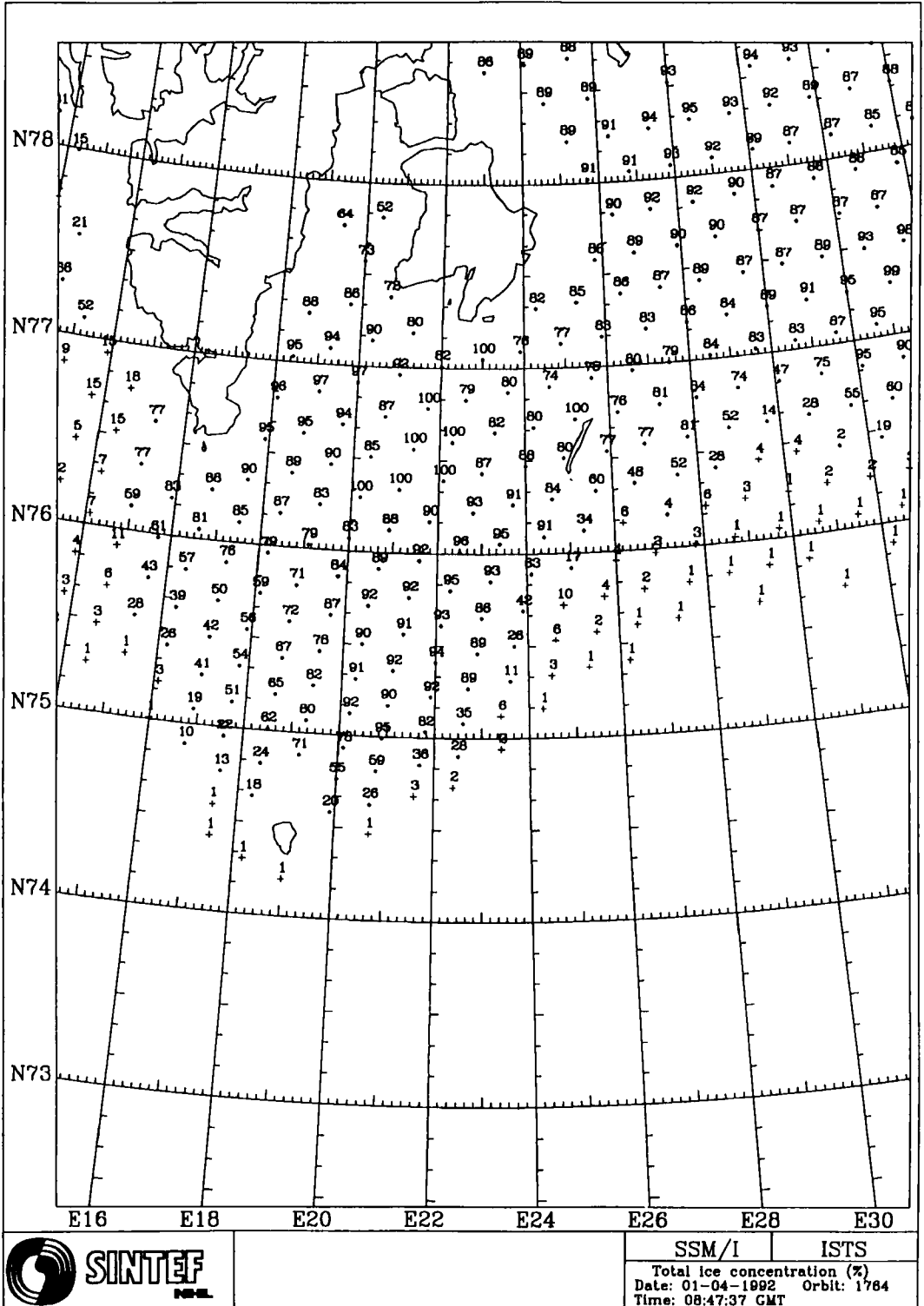
Fig. 8. SSM/I total ice concentrations (%, ●) and cloud coverage (/10,+) on 1 April 1992.

In addition to the SSM/I and AVHRR data sets listed in Table 1, three ERS-1 SAR scenes have been acquired (23, 26 and 29 March 1992) to study the ice conditions. Ground observations were performed during a vessel survey and several helicopter flights in the period 29 March–3 April. During the helicopter flights the ice conditions were monitored simultaneously by S-VHS Video and a FLIR camera mounted on the underside of the helicopter.

Fig. 5 shows the total ice concentrations on 26 March. The frame shows the location of the ERS-1 SAR scene and the location of the ice edge as observed in the SAR scene. The figure shows good agreement in ice edge position between the SSM/I and SAR data. This was also the case for the other two SAR scenes acquired. The SSM/I ice chart from 26 March shows more than 80 per cent total ice concentrations for most of the ice field. During the cold period, freezing occurred forming frazil, grease and pancake ice. The ice edge moved eastwards reaching an easterly maximum 1 April. On this day there were 30–50 km frazil/grease ice between the open water and the compacted pancake ice edge. The air temperature increased rapidly from 30 March to 3 April due to the winds turning eastwards and further southwards. Since the wind direction changed from office to on-ice, the newly formed ice was compressed and the ice edge moved westwards. The easterly winds led to an ice concentration close to 100 per cent from the ice edge into the ice field. During such conditions SSM/I seem to underpredict the ice concentrations slightly.

Observations on 26 March and 1 April 1992

To study brightness temperatures during different weather conditions the data from 26 March and 1 April 1992 are selected. The daily SSM/I ice charts monitored total ice concentrations and the location of the compacted ice edge very well.

Figs. 6 and 7 show the cloud percentages from LAM50S at 500 HPa level for 26 March and 1 April respectively. Despite the high cloud percentages the AES/YORK Algorithm detected the compacted ice edge position very well on both days. The ERS-1 SAR image from 26 March showed only a few kilometres of frazil ice outside the compacted ice edge. Hence, the frazil ice will have less influence on the brightness temperatures on this day than on 1 April where observations from helicopter showed frazil/grease ice up to
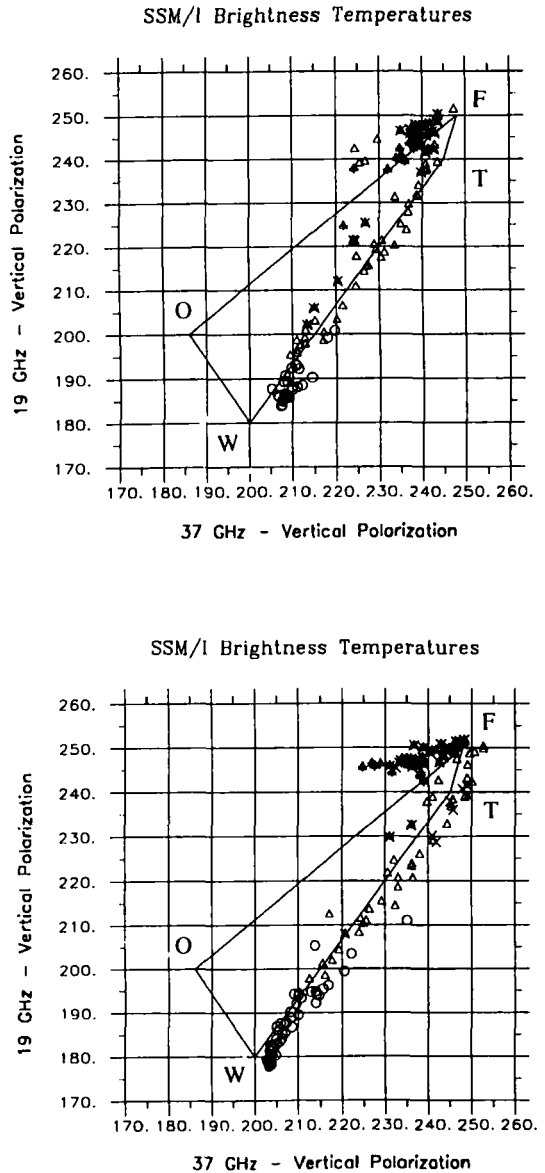

SSM/I Brightness Temperatures

SSM/I Brightness Temperatures

Fig. 9. Scatter plots of T_{v19} vs. T_{v37} for First Year Ice ($\triangle$), Old Ice (+), Thin Ice ($\times$) and Cloud Cover ($\bigcirc$) footprints in the area 74°N–77°N and 20°E–35°E 26 March (top) and 1 April (bottom) 1992. The polygon (OWTF) shows the valid area for ice footprints when no atmospheric contribution is present.

40–50 km outside the compacted ice edge. This frazil/grease ice area was not reported as ice by SSM/I, but was interpreted as cloud cover (Fig. 8)

Figs. 9 and 10 show scatter plots of T_{v19} vs. T_{v37} and T_{h37} vs. T_{v37} respectively for First Year Ice,
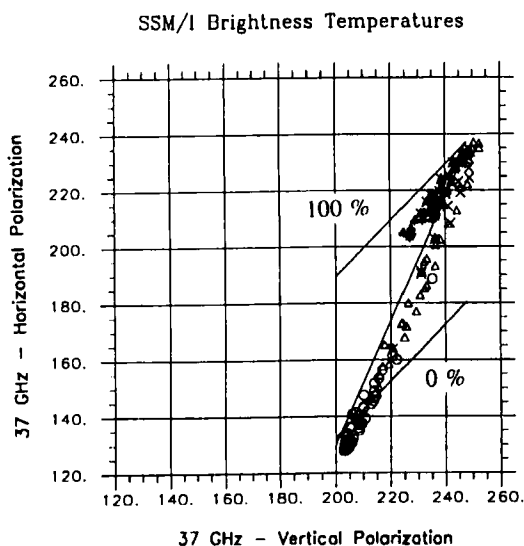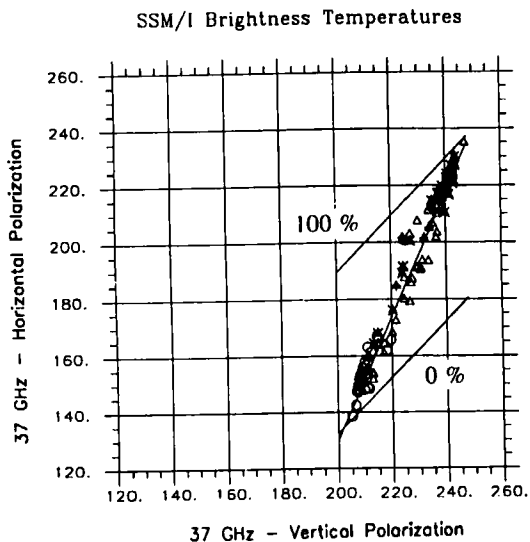
SSM/I Brightness Temperatures

37 GHz — Vertical Polarization

SSM/I Brightness Temperatures

37 GHz — Vertical Polarization

Fig. 10. Scatter plots of T_{h37} vs. T_{v37} for First Year Ice ($\triangle$), Old Ice (+), Thin Ice ($\times$) and Cloud Cover ($\bigcirc$) footprints in the area 74°N–77°N and 20°E – 35°E 26 March (top) and 1 April (bottom) 1992. The straight lines in the figures show the 0% and 100% total ice concentration lines and the WF line.

Old Ice, Thin Ice and Cloud Cover (over ocean) footprints in the area 74°N–77°N and 20°E–35°E on 26 March and 1 April 1992. The 37 GHz scatter plot from 26 March (Fig. 10 top) shows brightness temperatures along the WF line while the similar plot from 1 April (Fig 10. bottom) shows bright-

ness temperatures along a line offset from the WF line. This offset is due to weather effects and results in some ice points being classified as ice free and underprediction of ice concentration.

Discussion

This paper has presented the basic principals and equations for retrieval of sea ice parameters from spaceborne passive microwave observations and has outlined some of the atmospheric influence on the retrieval of sea ice information. Figures showing data from 26 March and 1 April 1992 show some of these effects. The AES/YORK algorithm detects the compacted ice edge very well. Also the total ice concentrations estimates are reliable. Frazil/grease ice outside the compacted ice edge may be interpreted as cloud cover. As such ice is of minor importance to navigation this misinterpretation is also of minor importance for navigational use of the sea ice information derived from SSM/I data.

The equations presented show that the brightness temperature from each satellite footprint can be split into three "ice" components; open water and two ice types. The most hazardous sea ice for navigation is old ice. Hence the AES/YORK algorithm first tests for old ice fraction. If the old ice criteria is met, the remaining ice fraction is the first year ice fraction. However, if no old ice is detected the algorithm calculates the fraction of first year and thin (new) ice. Changes in the weather (especially air temperature) may cause the algorithm to switch from identifying old ice one day to thin ice a day or two later (or vice versa). However, by following the changes in ice conditions from day to day such rapid changes in ice conditions will be revealed. If a satellite footprint is classified as ice free, cloud cover and wind speed information might be derived instead of ice fractions.

The data sets derived for this study have not yet been completely analysed and we expect to know more on how well regional climatological information can improve the interpretation of SSM/I data when this work is finished.

References

Basharinov, A. E., Gurvich, A. S., Yegorov, S. T., Kurskaya, A. A., Matveyev D. T. & Shutko, A. M. 1971: The results of microwave sounding of earth's surface according to exper-

imental data from Cosmos 243, Space Res., 11, Akademie-Verlag, Berlin.

Haroules, G. G. & Brown, W. E. 1969: The Simultaneous Investigation of Attenuation and Emission by the Earth's Atmosphere at Wavelengths from 4 cm to 8 mm. *J. Geophys. Res. 74*, 4453–4471.

Hollinger, J., Lo, R. & Poe, G. 1987: Special Sensor Microwave Imager User's Guide. Naval Research Laboratory Report.

Hollinger J. 1991: DMSP special sensor microwave/imager calibration/validation. Final Report: Vol. II, NRL, Washington, D.C.

Løvås, S. M., Vefsnmo, S. & Ramseier, R. O. 1991: Barents Sea Ice Conditions as observed by Passive Microwave and other techniques. *2nd WMO Operational Ice Remote Sensing Workshop, September 10–13, 1991, Ottawa, Ontario, Canada.*

Ramseier, R. O., Lapp, D., Rubinstein, I. G. & Asmus, K.

1989: Canadian Validation of the SSM/I and AES/York Algorithms for Sea Ice Parameters. ISTS/Microwave Group Report.

Rubinstein, I. G. 1986: Selection of temperature independent dual frequency sea ice algorithm. Ph. D assoc. report for AES. Toronto, Ontario. 155 pp.

Staelin, D. H., Barett, A. E., Waters, J. W., Barath, F. T., Johnston, E. J., Rosenkrantz, P. W., Grant, N. E., & Lenoir, W. R. 1973: Microwave spectrometer on the Nimbus-5 satellite, meteorological and geophysical data. *Science 182*, 1339–1341.

Swift, C. T., Fedor, S. & Ramseier, R. O. 1984: An algorithm to measure sea-ice concentrations with microwave radiometers. *J. Geophys. Res. 90*, 1087–1099.

Zwally, H. J. 1984: Observing Polar Ice Variability. *Annals of Glaciol. 5*, 191–198.